AGU PUBLICATIONS

Tectonics

RESEARCH ARTICLE
10.1002/2016TC004231

Key Points:
- New geo-thermochronological data set along a 400 km long trench-parallel profile
- Southern Peruvian fore-arc deformation history and its linkage to oroclinal bending
- Crustal-scale block tilting occurs contemporaneously to oroclinal bending

Supporting Information:
- Supporting Information S1

Correspondence to:
M. Noury,
melanienoury@gmail.com

Citation:
Noury, M., M. Bernet, T. F. Schildgen, T. Simon-Labric, M. Philippon, and T. Sempere (2016), Crustal-scale block tilting during Andean trench-parallel extension: Structural and geo-thermochronological insights, *Tectonics*, *35*, 2052–2069, doi:10.1002/2016TC004231.

Received 10 MAY 2016
Accepted 28 JUL 2016
Accepted article online 31 JUL 2016
Published online 17 SEP 2016

Crustal-scale block tilting during Andean trench-parallel extension: Structural and geo-thermochronological insights

M. Noury[1,2,3], M. Bernet[1,3], T. F. Schildgen[4,5], T. Simon-Labric[1,6], M. Philippon[2], and T. Sempere[1,3,7]

[1]ISTerre, Université Grenoble-Alpes, Grenoble, France, [2]Géosciences Montpellier, Université des Antilles, Pointe-à-Pitre, France, [3]ISTerre, CNRS, Grenoble, France, [4]Institut für Erd- und Umweltwissenschaften, Universität Potsdam, Potsdam, Germany, [5]Helmholtz Zentrum Potsdam, GeoForschungsZentrum (GFZ) Potsdam, Potsdam, Germany, [6]Musée des Minéraux, Centre de Géologie de l'Oisans, Bourg d'Oisans, France, [7]ISTerre, IRD, Le Bourget du Lac, France

Abstract Despite a long history of plate convergence at the western margin of the South American plate that has been ongoing since at least the Early Paleozoic, the southern Peruvian fore-arc displays little to no evidence of shortening. In the light of this observation, we assess the deformation history of the southern Peruvian fore-arc and its geodynamic implications. To accomplish this, we present a new structural and geo-thermochronological data set (zircon U-Pb, mica $^{40}Ar/^{39}Ar$, apatite and zircon fission-track and zircon (U-Th)/He analyses) for samples collected along a 400 km long transect parallel to the trench. Our results show that the Mesoproterozoic gneissic basement was mainly at temperatures ≤350°C since the Neoproterozoic and was later intruded by Jurassic volcanic arc plutons. Along the coast, a peculiar apatite fission-track age pattern, coupled with field observations and a synthesis of available geological maps, allows us to identify crustal-scale tilted blocks that span the coastal Peruvian fore-arc. These blocks, bounded by normal faults that are orthogonal to the trench, suggest post-60 Ma trench-parallel extension that potentially accommodated oroclinal bending in this region. Block tilting is consistent with the observed and previously described switch in the location of sedimentary sources in the fore-arc basin. Our data set allows us to estimate the cumulative slip on these faults to be less than 2 km and questions the large amount of trench-parallel extension suggested to have accommodated this bending.

1. Introduction

The western margin of South America marks one of the oldest active subduction zones in the world. This setting gave rise to the Central Andes, a mountain belt characterized by the occurrence of the second largest elevated plateau in the world, the Altiplano-Puna, which shows a broad curvature known as the Bolivian Orocline (Figure 1, inset). The Andean cordillera contrasts with other major orogens such as the Alps or Himalayas because it does not result from the collision of two continental plates but from the subduction of the Nazca oceanic plate below the South American continental plate. Moreover, no terrane accretion occurred between 15 and 18°S since ~480 Ma [e.g., *Ramos and Aleman*, 2000]. This portion of the active margin, and in particular its fore-arc, is thus ideal to study the evolution of the upper plate over a long period of time.

The dominant paradigm in the Central Andes postulates that crustal thickening mostly resulted from contractional tectonics, which is believed to have propagated from west (fore-arc) to east (Subandes) since the Late Cenozoic [*Isacks*, 1988; *Suárez et al.*, 1983]. However, in southern Peru, the upper crust of the fore arc is characterized by widespread extensional and strike-slip deformation episodes of various ages from Late Paleozoic to Cenozoic [*Sébrier et al.*, 1985; *Sempere et al.*, 2004; *Roperch et al.*, 2006; *Schildgen et al.*, 2009], whereas there is little to no evidence of shortening [*James*, 1971; *Myers*, 1975; *Mégard*, 1978; *Tosdal et al.*, 1984; *Kono et al.*, 1989; *James and Sacks*, 1999; *Rochat et al.*, 1999; *Sempere and Jacay*, 2006, 2007, 2008]. Few trench-parallel thrusts are reported in the Central Andean fore-arc and have been described either as dipping to the southwest bounding a tectonic nappe [*Moores and Twiss*, 1995] or to the northeast defining the western boundary of the bivergent Andean orogen [*Armijo et al.*, 2015]. However, it is not excluded that these thrusts are flower structures formed along strike-slip faults that were active during the formation of the Bolivian Orocline [*Jacay et al.*, 2002; *Flores et al.*, 2005; *Hall et al.*, 2012].

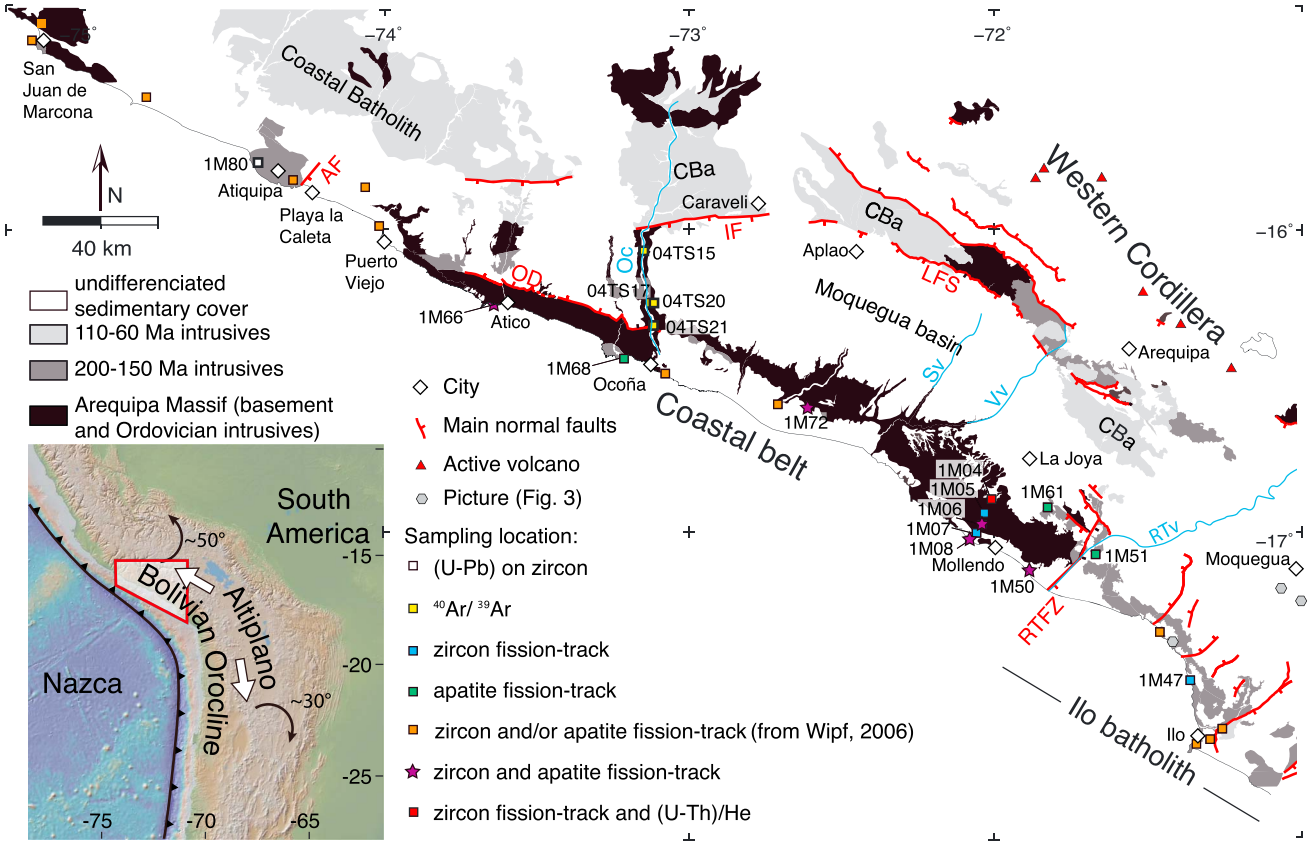

Figure 1. Synthetic geological and structural map of the Southern Peruvian fore arc showing the three groups of intrusive rocks cropping out in the study area. Red text: AF: Atiquipa Fault, CBa: Coastal Batholith, IF: Iquipi fault, LFS: Llucla normal Fault System, RTFZ: Río Tambo Fault Zone; OD: Ocoña Detachment. Blue text SV: Siguas valley, Vv: Vitor valley, Oc: Ocoña canyon, RTv: Rio Tambo valley. Samples location from this study (squares) and *Wipf et al.* [2008] (stars) are indicated. The inset shows the Bolivian Orocline, the Altiplano, and the location of the study area (red polygon). The amount of rotation from *Arriagada et al.* [2008] is also indicated as well as the principal direction of stretching resulting from these differential and opposite rotations of the northern and southern parts of the orocline during bending (white arrows).

Indeed, important counterclockwise rotations of rigid blocks around their vertical axis occurred in the southern Peruvian fore-arc between ~40 and ~20 Ma [*Roperch et al.*, 2006]. *Arriagada et al.* [2008] proposed a 2-D paleogeographic reconstruction of the margin and calculated that the oroclinal bending was accompanied by ~200 to 260 km of stretching parallel to the trench between ~10°S and ~30°S (Figure 1, inset). Although various normal faults that strike perpendicular to the coastline [*Bellido and Guevara.*, 1963; *Narvaez*, 1964; *Roperch et al.*, 2006] may have accommodated this extension, the influence of block rotation on the exhumation history of the rocks exposed at the surface today is poorly documented in the fore-arc, where vertical axis rotations can reach ~55° [*Arriagada et al.*, 2008].

Studies investigating the Neogene exhumation history of the present-day fore-arc of southern Peru [*Schildgen et al.*, 2007; *Schildgen et al.*, 2009; *Gunnell et al.*, 2010; *Wipf et al.*, 2008] yielded a wide range of thermochronologic ages: ~5 Ma to 75 Ma for the apatite (U-Th)/He system and 50 to 105 Ma for the apatite fission-track system. Rock cooling histories reconstructed from these data show that most of the denudation had occurred before 24 Ma and that surface uplift-driven incision of the Ocoña valley (Figure 1) occurred after 14 Ma [*Schildgen et al.*, 2007; *Schildgen et al.*, 2009; *Gunnell et al.*, 2010]. In this study, we assess the deformation history and its potential linkage to oroclinal bending in the fore-arc during the Paleogene. We focus on the fore-arc of southern Peru between ~14°S and ~17°S, where block rotation was the most important [*Arriagada et al.*, 2008] (Figure 1, inset). We characterize the thermal evolution of the fore-arc by using five different thermochronometers (zircon U-Pb, mica $^{40}Ar/^{39}Ar$, zircon and apatite fission tracks, and zircon (U-Th)/He), comprising both new and published data. Combined with field data and a synthesis of available geological maps, this approach allows us to describe postcooling tilting of blocks due to orogen-parallel extension accommodated on faults that strike perpendicular to the coastline. Together with the sedimentary

architecture of the Cenozoic fore-arc deposits, we better constrain offset on the faults and their timing of activity with respect to bending of the Bolivian Orocline.

2. Geological Setting of the Peruvian Forearc

2.1. Basement

2.1.1. Proterozoic Schists, Gneiss, and Granulites

The present-day fore-arc of southern Peru provides the best exposed Proterozoic basement inlier of the South American Pacific coast, the Arequipa Massif [*Cobbing and Pitcher*, 1972] (Figure 1, black color). It is exposed along ~600 km of coastline between ~14°S and ~17°S, and outcrops extend from the sea cliffs of the Coastal Belt to ~100 km inland in the Coastal Batholith (Figure 1). The Arequipa Massif is composed of ultrahigh temperature (>900°C) Proterozoic granulites between ~17 and ~16.5°S [*Martignole and Martelat*, 2003; *Loewy et al*., 2004; *Casquet et al*., 2010] and gneisses in the Coastal Batholith and northwest of ~16.5°S. Gneisses are unconformably overlain in the San Juan de Marcona area (~15.5°S) by the Upper Neoproterozoic, glaciogenic Chiquerio Formation, which experienced greenschist facies metamorphism during the Early Paleozoic [*Chew et al*., 2007; *Chew and Kirkland*, 2011].

2.1.2. Volcanic Arc Intrusives and Deposits

The study area has been located above a major subduction zone since at least the Early Paleozoic, and possibly since ~650 Ma [*Chew et al*., 2007]. As a result, Phanerozoic rocks overlie and are intruded into the Arequipa Massif. Ordovician-Silurian subduction-related granitoid intrusions are exposed between 16.25°S and 17°S [*Loewy et al*., 2004; *Casquet et al*., 2010], and Carboniferous to Triassic fore-arc deposits outcropping mainly near Atico and Ocoña overlie the Arequipa Massif (Figure 1, white color) [*Narvaez*, 1964; *Bellido and Guevara*, 1963; *Sempere et al*., 2012; *Boekhout et al*., 2013]. Magmatic activity has been almost continuously active along the margin of southern Peru since at least the Early Jurassic [*Demouy et al*., 2012; *Boekhout et al*., 2012], although the volcanic arc has migrated over time [*Mamani et al*., 2010]. Three phases of migration are described: (1) toward the SW between ~200 and ~150 Ma, then (2) toward the NE between ~110 and ~30 Ma, and then again (3) toward the SW since 30 Ma [*Mamani et al*., 2010]. Lower Jurassic (200–175 Ma) and Upper Jurassic (175–150 Ma) plutons intruded the gneissic basement of the Arequipa Massif (Figure 1, black color) forming the Coastal Batholith (in the Arequipa area, ~30 km inland from the coastline) and the Ilo Batholith (south of 17.1°S), respectively (Figure 1, grey color). These plutons were themselves intruded by Upper Cretaceous to Paleocene (90–60 Ma) and Lower Cretaceous (110–106 Ma) plutons forming the composite Coastal and Ilo Batholith, respectively [*Demouy et al*., 2012; *Boekhout et al*., 2012] (Figure 1, light grey color). Thus, these composite Batholiths, striking parallel to the trench, recorded the two first stages of this migration (Figure 1).

Volcanic arc products of Jurassic to Lower Cretaceous age overlie the Arequipa Massif and the Ordovician to Cretaceous intrusive rocks and are mainly located near Atiquipa, north of Ilo, and in the main river valleys [e.g., *Roperch et al*., 2006]. Additionally, a sedimentary succession of ~185–50 Ma marine back-arc deposits outcrops ~50 km northeast of Aplao and ~50 km southeast of Arequipa [*Jenks*, 1948; *Sempere et al*., 2002; *Boekhout et al*., 2013]. At map scale, these arc-related plutonic and volcanic rocks crop out in the core of trench-parallel horsts (Figure 1, white color).

2.2. Moquegua Basin

The Moquegua basin [*Marocco*, 1984; *Sempere*, 2000; *Roperch et al*., 2006; *Decou et al*., 2011, 2013] unconformably overlies the aforementioned basement and crops out between Caravelí and La Joya (Figure 1). These mostly continental fore-arc sediments of Eocene to Pliocene age clearly prograde seaward and were deposited between ~50 and ~4.5 Ma [*Roperch et al*., 2006]. The Moquegua Group is subdivided into four units, from the Moquegua A (MoqA) at the base to Moquegua D (MoqD) at the top [*Sempere et al*., 2004; *Roperch et al*., 2006]. A detailed map of these deposits (grouping Moquegua A and B) is shown in our compiled structural map (Figure 2). This basin is described as a foreland-type basin of the Western Cordillera [*Armijo et al*., 2015].

Close to Caravelí, Moquegua A/B deposits are composed of coarse fluvial conglomerates that evolve toward the SW through microconglomerates close to Aplao to fine-grained sandstones intercalated with gypsiferous strata close to Moquegua [*Roperch et al*., 2006]. In contrast to the Moquegua A/B succession, Moquegua C deposits are mainly composed of tuffaceous volcanic strata. The base of these deposits is estimated at ~30 Ma [*Roperch et al*., 2006], and the sedimentary facies is increasingly proximal toward the SE. Indeed, in

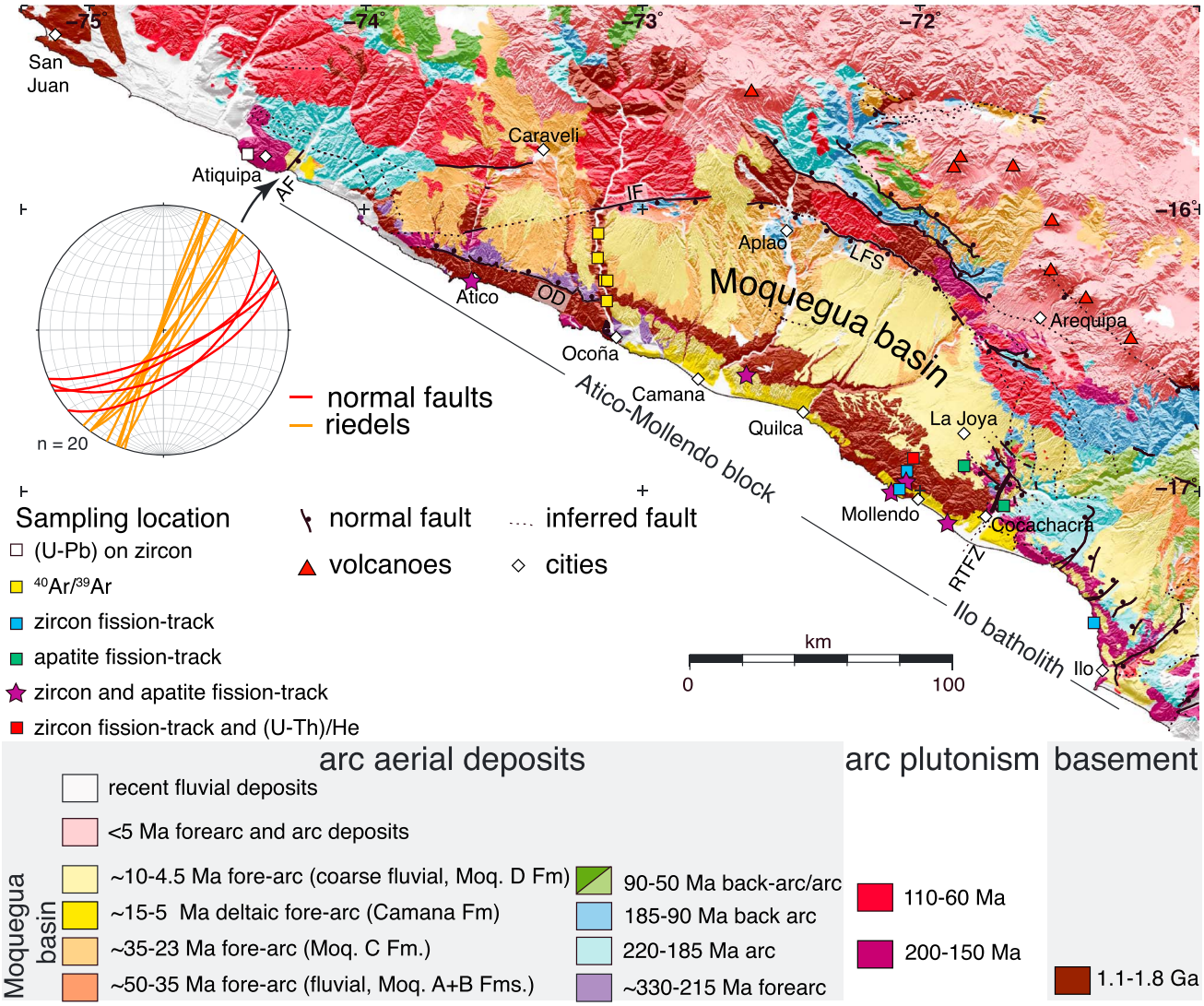

Figure 2. Synthetic geological and structural map of the study area showing the Neoproterozoic basement, the arc-related plutons and the arc-related aerial deposits. The white triangles display the present-day Andean arc. AF: Atiquipa Fault, IF: Iquipi Fault, LFS: Lluclla normal Fault System, RTFZ: Río Tambo Fault Zone, OD: Ocoña Detachment. Squares indicate the sample sites. The stereogram, Schmidt projection lower hemisphere, shows field measurement of the Atiquipa Fault (red planes) and its associated riedels (orange planes).

the Caravelí area, a marine incursion is recorded by the "Caravelí limestones," which are interbedded with volcanic products dated at 25 Ma [*Noble et al.*, 1985], whereas numerous fluvial conglomerates are intercalated within the tuffs in the Siguas valley (Figure 1). Moreover, these deposits clearly bevel toward the SE and are totally absent in the Vitor Valley (Figure 1). Moquegua D deposits, composed of coarse continental conglomerates, unconformably overlie previous Moquegua units.

2.3. Major Structures

The strain pattern of the study area shows two directions of faults: normal and parallel to the trench (Figure 1). The kinematics (normal or reverse) of these faults are still debated. For example, the Moquegua basin is bounded by a major fault, the Lluclla fault, that trends parallel to the trench (Figure 1), which has been interpreted either as normal [*Sébrier et al.*, 1985; *Demouy et al.*, 2012] or reverse [*Armijo et al.*, 2015]. In addition, several faults strike perpendicular to the coastline. One major structure is the Río Tambo Fault System, which was described by *Roperch et al.* [2006] as a dextral fault zone with 60 km of offset. Lateral variations in the geologic units on either side of the Río Tambo valley attest that the valley marks a major structural feature [*Roperch et al.*, 2006]. Indeed, the metamorphic grade of

Proterozoic rocks increases toward the southeast between Puerto Viejo and the Río Tambo valley (i.e., latitudes 15 to 17°S) [*Martignole and Martelat*, 2003]. Other trench-perpendicular faults have been mapped between 17 and 18°S by the Instituto Geológico Minero y Metalúrgico (INGEMMET) [*Bellido and Guevara*, 1963; *Narvaez*, 1964].

3. Materials and Methods

In this study we present new thermochronologic data to better constrain the cooling history of the Coastal Belt of southern Peru (Figure 1). We focused our sampling on a 400 km long profile along the Coastal Belt, composed of ultrahigh-temperature migmatites intruded by Ordovician and Jurassic plutons. To perform apatite and zircon fission-track analyses and zircon U-Pb and (U-Th)/He dating, several kilograms of rock specimens were crushed, and apatite and zircons were extracted from the 100–200 μm size fraction by using standard magnetic and heavy liquid separation techniques. Not all samples yielded enough apatites and/or zircons to carry out analyses. As a result, samples from a total of 17 localities (Figure 1) could be analyzed, including 12 for apatite and zircon fission-track analysis (three samples yielded enough apatite and zircon to carry out both techniques on these samples), one for zircon (U-Th)/He dating, and four for $^{40}Ar/^{39}Ar$ dating on biotite and muscovite. Ten samples were collected from the Proterozoic basement, four from Ordovician plutonic rocks, and two from granitoids of unknown crystallization age on which we also performed zircon U-Pb analyses.

3.1. Fieldwork and Synthesis of Preexisting Maps

For this study a detailed structural map has been constructed from available geological maps at the 1:100,000 scale published by the INGEMMET, satellite pictures available within *Google Earth* [2014], SRTM data, and our own field observations.

3.2. Zircon U-Pb Dating

Zircons extracted from the Atiquipa monzonite were dated by using the U-Pb laser ablation inductively coupled plasma–mass spectrometry (ICP-MS) method. Zircon grains were mounted into epoxy resin blocks and polished to obtain flat surfaces. The zircon grains were characterized by cathodoluminescence imaging on a Hitachi S-2500 scanning electron microscope (ISTerre, University Grenoble-Alpes, France) to reveal their internal structure. $^{206}Pb/^{238}U$ and $^{207}Pb/^{235}U$ dates were obtained by using a 193 nm excimer ablation system UP-193FX coupled to an Element XR sector field, single collector ICP-MS (Thermo Scientific) at the Institute of Mineralogy and Geochemistry, University of Lausanne. Operating conditions were similar to those described in *Ulianov et al*. [2012]. Analyses were performed on the 16 grains available by using a 35 μm spot size focused on external zircons growths rims combined with a relatively low on-sample energy density of ~3 J/cm^2 and a repetition rate of 5 Hz to minimize fractionation. A GJ-1 standard zircon (CA–ID–TIMS Pb^{206}/U^{238} age of 600.5 ± 0.4 Ma) [*Boekhout et al*., 2012] was used for external standardization. The Plesoviče zircon standard was measured along with sample zircons on a routine basis to control. No common lead correction was applied due to the presence of ^{204}Hg in the system.

3.3. $^{40}Ar/^{39}Ar$ Dating

Fresh biotite and muscovite crystals were handpicked from the 500–1000 μm size fraction of crushed bedrock samples. Crystals were ultrasonically cleaned in high-purity water and ethanol, ground in a mortal and pestal to remove altered grain edges, and ultrasonically cleaned a second time prior to packaging in Al foil packets. All samples were encapsulated in quartz vials for irradiation at the McMaster University reactor along with flux monitor Fish Canyon Tuff sanidine (28.02 Ma) [*Renne et al*., 1998] and synthetic salts to permit corrections for interfering nuclear reactions. Vertical monitoring of the neutron flux resulted in J values known to better than 0.2 to 0.3%.

Gas was liberated from crystals after incremental heating of the packet in a vacuum furnace. Plateau dates were calculated by using three or more consecutive steps with overlapping uncertainty comprising at least 50% of the total $^{39}Ar_K$ released. The evolved gas was purified with a series of metal alloy getters and analyzed on the Massachusetts Institute of Technology MAP 215-50 mass spectrometer with an electron multiplier. Total system blanks were measured at the beginning of each analytical session and between sets of two to six incremental heating analyses depending on blank reproducibility. Mass fractionation was monitored by

routine analysis of laboratory air over the duration of the analysis. Isotopic measurements were reduced by using the ArArCALC routines of *Koppers* [2002] and corrected for system blanks, mass fractionation, and neutron-induced interferences. Apparent $^{40}Ar/^{39}Ar$ ages were calculated by using decay constants recommended by *Steiger and Jäger* [1977], assuming an initial $^{40}Ar/^{36}Ar$ ratio of 295.5. Age uncertainties include errors associated with blank and sample isotopic measurements, fractionation, interfering reactions, and J. For samples with weighted mean dates characterized by a MSWD (mean square weighted deviate) > 1, scatter is assumed to be greater than the contribution from analytical errors, and errors were multiplied by the square root of the MSWD [*York*, 1969].

3.4. Zircon (U-TH)/He Dating

Zircon grains were hand-picked from the 100 to 200 μm size fraction to select idiomorphic and inclusion-free specimens. (U-Th)/He analyses were performed at the University of Arizona, following the method described by *Reiners et al*. [2004]. All aliquots consist of a single grain for which abundance of He was measured by laser mass spectrometry. The concentrations of U and Th were measured by isotope dilution. An α-ejection correction (*Ft*) was applied to each crystal to derive a corrected (U-Th)/He age [*Reiners*, 2005].

3.5. Apatite and Zircon Fission Track Dating

Apatites and zircons were mounted in epoxy resin and Teflon® sheets, respectively, and polished to expose an internal surface for each grain. Apatites were then etched with a 5.5 mol HNO_3 for 20 s at 21°C. Zircons were etched in a NaOH-KOH melt between 19 and 56 h at 228°C. We used the external detector method for fission-track analysis. Apatite and zircon grain mounts were thus covered with uranium-poor muscovite sheets as external detectors and irradiated at the FRM II reactor at Garching, Germany. Apatite samples were irradiated with a nominal fluence of 4.5×10^{15} n/cm^2 together with Fish Canyon Tuff and Durango apatite age standards and with IRMM540R (15 ppm) dosimeter glasses. Zircon samples were irradiated with a nominal fluence of 0.5×10^{15} n/cm^2 together with Fish Canyon Tuff and Buluk Tuff age standards and CN1 (39.8 ppm) dosimeter glasses. After irradiation, the muscovite detectors of all mounts were etched for 18 min in 48% HF at 21°C to reveal induced tracks. Spontaneous and induced fission tracks were counted at the ISTerre fission-track laboratory, Grenoble University, France, at 1250× magnification by using a dry objective and an Olympus BX51 microscope and the FTStage 4.04 system [*Dumitru*, 1993]. Only crystals with polished surfaces parallel to the crystallographic *c* axis were considered. The individual grain ages as well as the pooled and mean ages were calculated as recommended by *Galbraith* [2005]. To compute central ages, we used the RadialPlotter software [*Vermeesch*, 2009, 2012].

4. New Structural Map of the Southern Peruvian Fore-Arc

Our new structural map of the Peruvian fore-arc basement and basin (Figure 2) highlights the geological structure of the study area and more specifically the relationships between basement units and the Moquegua basin. We combined units that had previously been mapped separately: apart from the basement and the Carboniferous fore-arc deposits, we choose to differentiate three periods of time: ~200–150 Ma, 110–30 Ma, and 30–0 Ma. These periods correspond to different directions of arc migration [*Mamani et al*., 2010]: toward the NE between 110 and 45 Ma and toward the SW from 200 to 110 Ma and since 45 Ma. For each of these periods, we distinguish rocks formed in arc (plutonic or volcanic), fore-arc, and back-arc contexts (Figure 2).

Our map illustrates that the Moquegua basin is a half-graben controlled at its northwestern boundary by the ~230 km long, mainly trench-parallel Lluclla normal Fault System (LFS) (Figures 1 and 2) [*Sébrier et al*., 1985; *Roperch et al*., 2006; *Schildgen et al*., 2009; *Demouy et al*., 2012]. From west to east, the longitudinal increase of the basin width suggests a scissor-like opening. Moquegua basin deposits onlap the basement, bevelling toward the SW, and thus represent a depocenter of the LFS. The Coastal Belt forms the basin's southwestern boundary. It consists of a trench-parallel trending (<20 km wide) strip of basement that crops out as an ~1000 m high coastal cliff (Figure 2).

Numerous normal faults affected the Moquegua basin deposits (MoqA, B, C and D Formations) during its formation (Figure 3). The MoqA/B red sandstone deposits were highly deformed by NNE-SSW trending normal faults, mainly after their deposition (Figure 3a). This mainly WNW-ESE extensional episode was active during deposition of the MoqC tuffaceous sandstones (from 30 to 10 Ma) as evidenced by the numerous synsedimentary structures that affect this formation (Figure 3b). Albeit less pervasive, extension

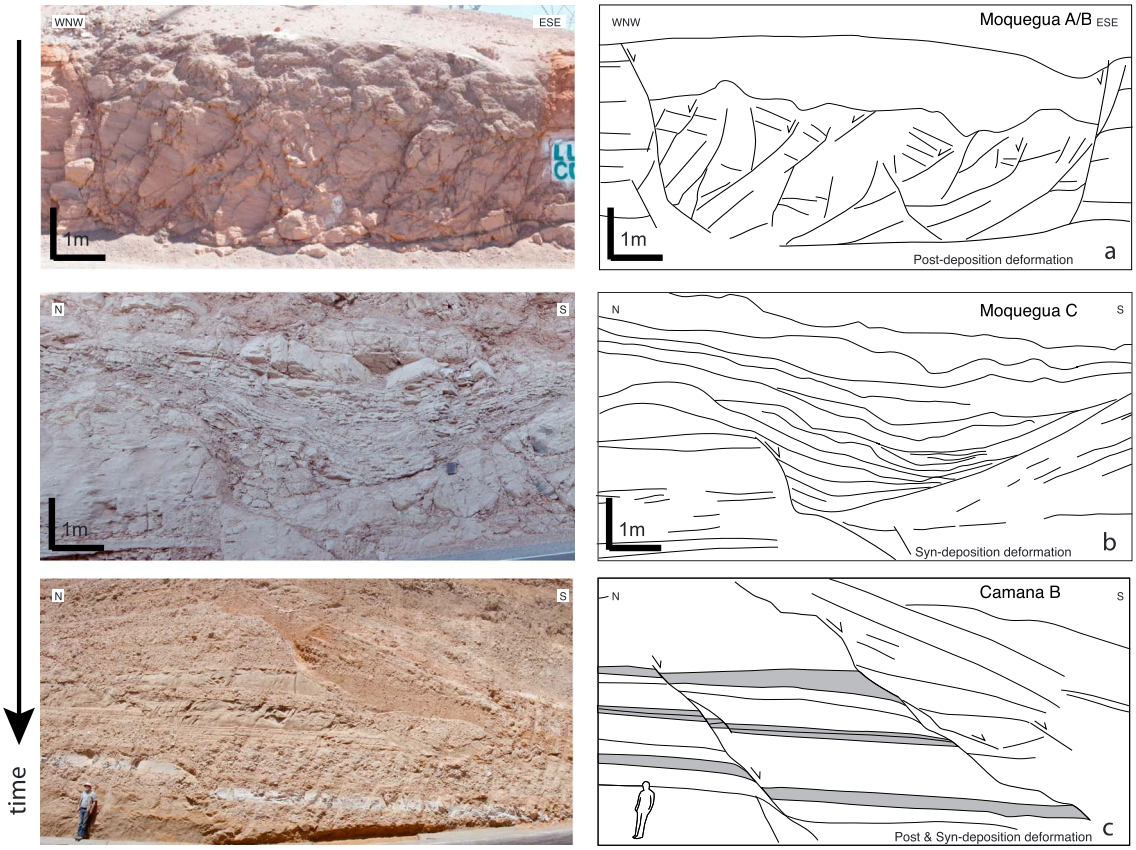

Figure 3. Field photographs showing the deformation pattern observed in the sedimentary archives of the Moquegua basin; the pictures are marked on Figure 1. (a) Graben affecting Moq A/B (red sandstones) and C (tuffaceous sandstones) deposits bounded by two oppositely dipping ENE-WSW trending normal faults with a meter-scale vertical offset; sediments are highly fractured. (b) Synkinematic growth strata in the Moq C tuffaceous sandstones affected by E-W trending and southward dipping normal faults with a several meters vertical offset. (c) Pliocene sandstones and conglomerates affected by E-W trending and southward dipping normal faults with a metric vertical offset.

continued during the late Miocene and Pliocene, as shown by a few E-W trending normal faults affecting the Camaná B marine deposits (Figure 3c), which are the coastal equivalents of the MoqD continental deposits [*Roperch et al.*, 2006].

Several faults strike perpendicular to the trench. Near Atiquipa, we mapped the Atiquipa normal fault that was previously undescribed (Figure 2). It outcrops at "Playa La Caleta" along the Panamerican highway and consists of an ~50 m thick fault breccia that affects the Atiquipa diorite on its southeastern border. We dated the crystallization of this diorite by zircon U-Pb method at 162.2 ± 1.1 Ma (Table S1 in the supporting information). The Atiquipa fault strikes N030° with subvertical to 60° dip toward the SE (stereogram; Figure 2). No kinematic indicators have been observed, but in the hanging wall of this fault zone, a conglomerate striking N170° and dipping 40°E suggests a drag fold. This conglomerate is itself affected by several normal faults striking broadly N60° and dipping 60°SE. Farther southeast, the Río Tambo fault zone [*Roperch et al.*, 2006]

Table 1. $^{40}Ar/^{39}Ar$ Analyses Results[a]

Sample Name	Latitude (°S)	Longitude (°W)	Altitude (m)	Mineral Dated	Age (Ma)	2σ Error (Ma)
04TS15	16.058445	73.168030	319	biotite	816.74	4.27
04TS17	16.225813	73.149583	275	biotite	483.1	5.45
04TS20	16.227267	73.144233	680	biotite	470.33	2.71
04TS21	16.301944	73.135556	100	biotite	468.1	2.62
04TS20	16.227267	73.144233	680	muscovite	467.67	2.60

[a]All samples are from Precambrian gneiss and were analyzed according to the protocol described in text.

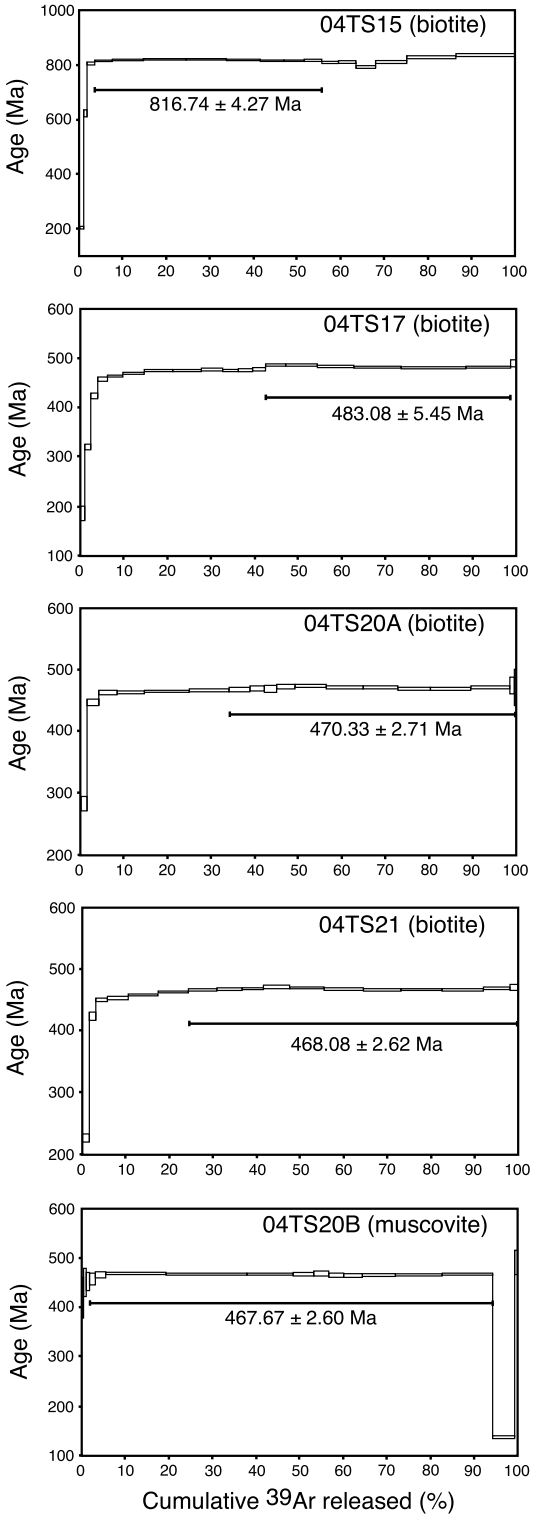

Figure 4. $^{40}Ar/^{39}Ar$ age spectra for samples from the Ocoña Canyon.

separates the ultrahigh-temperature migmatites of the Arequipa Massif to the northwest from the Ilo Batholith intruded in Jurassic strata to the southeast (Figure 2 and section 2.3).

Hereafter, the Atico-Mollendo block refers to the crustal block bounded to the northwest by the Atiquipa fault zone and to the southeast by the Río Tambo fault zone (Figure 2). Within this block, the basement exhibits a whole crustal section from sediments in the NW to ultrahigh-temperature migmatites in the SE [*Chew et al.*, 2007; *Martignole and Martelat*, 2003].

5. New Age Constraints Along the Coastal Southern Peruvian Forearc

5.1. Basement

5.1.1. Neoproterozoic Cooling and Ordovician Thermal Event

Four $^{40}Ar/^{39}Ar$ step-heating analyses have been performed on biotite and one on muscovite (Table 1) from the Ocoña canyon between the coast and the Iquipi fault ~50 km upstream (Figure 1). All samples exhibit well-defined plateau ages (Figure 4), ranging from 816.7 ± 4.3 Ma upstream to 468.1 ± 2.6 Ma downstream (~15 km from the outlet). An important shift in cooling ages is observed between 35 and 25 km from the river outlet, where biotite $^{40}Ar/^{39}Ar$ ages change from 816.7 ± 4.3 Ma (04TS15) to 468.1 ± 2.6 Ma (04TS21). Additionally, we sampled two gneisses in the canyon separated by ~500 m of elevation ~25 km from the outlet. Biotite $^{40}Ar/^{39}Ar$ analyses yielded an age of 483.1 ± 5.5 Ma for the lower sample (04TS17) and 470.3 ± 2.7 Ma for the upper sample (04TS20). Moreover, we obtained a muscovite $^{40}Ar/^{39}Ar$ age of 467.7 ± 2.6 Ma for the upper sample (Table 1).

5.1.2. Jurassic Fast Cooling

Zircon (U-Th)/He analysis of sample 1 M04 (Figure 1 and Table 2), a migmatite at 1200 m elevation, yielded a mean age of 158.6 ± 6.6 Ma. This age is within the 2σ uncertainty of the zircon fission-track age (149 ± 39 Ma; Table 3) obtained on the same sample. This sample did not yield enough apatite grains to perform apatite fission-track analyses but suggests Jurassic fast cooling from ~220°C to ~180°C (Figure 5). This fast cooling is consistent with the fact that five samples (1 M04 to 1 M08) along a profile located

Table 2. Analytical Data for (U-Th)/He on Zircon Age Determinations From Sample 1 M04

Sample	Grain Morphology	4He (nmol/g)	U (ppm)	Th (ppm)	eU (ppm)	Rs (um)	Corrected Age (Ma)	±2 s (Ma)
1 M04z1	abraded	50.42	40.2	132.4	71.3	66.4	163.2	1.8
1 M04z2	very abraded	53.75	56.6	99.4	79.9	68.9	153.9	1.9

~10 km NW of Mollendo across the coastal escarpment (Figure 1) and sampled at ~250 m elevation increments from the coastline to 1200 m elevation yielded equivalent zircon fission-track ages within 2σ uncertainty (Table 3 and Figure 5).

5.1.3. Cooling Age Pattern Parallel to the Coast

In this section, we will illustrate the coast-parallel variations in thermochronological ages by projecting ages obtained in this study and previously published data [*Wipf et al*., 2008] onto a line parallel to the coast (Figure 5). The seven zircon fission-track ages obtained along the coast range between 244 ± 62 Ma and 61 ± 13 Ma. Apatite fission-track ages range from 93 ± 28 Ma (1 M51) to 63 ± 10 Ma (1 M50) (Table 4 and Figure 5). Every sample analyzed with the fission-track method passed the chi-square test [*Green*, 1981] except zircons of sample 1 M50 (Table 3). This means that obtained central ages are calculated from a single population. However, due to the low uranium content in the apatites, it was not possible to measure a significant number of confined horizontal track lengths in these samples, nor in the samples from the Mollendo transect crosscutting the Coastal Belt in the south (Figure 1). Therefore, we decided not to model time-temperature histories.

Thermochronologic ages available for the study area are compiled in Table S2. In particular, of the six previously published apatite (U-Th)/He ages available, four are between 59 and 72 Ma and two are younger at 24.6 ± 12 Ma and 29 ± 7 Ma. Apatite fission-track ages cluster around ~60 to 70 and ~90 to 100 Ma, without any obvious relationship between central fission–track ages and mean track-length [*Wipf*, 2006]. Zircon (U-Th)/He ages are ~150 to ~180 Ma, whereas zircon fission-track ages are widely dispersed between 61 ± 13 and 531 ± 99 Ma. These data thus document very slow long-term exhumation rates in this area [*Wipf*, 2006; *Schildgen et al*., 2007; *Wipf et al*., 2008; *Schildgen et al*., 2009]. In the domain intruded by the Ilo Batholith, SE of the Río Tambo fault zone, apatite fission-track ages cluster between ~85 and 95 Ma. They are slightly younger than the two available zircon fission-track ages that are equivalent to zircon crystallization ages (110–106 Ma; Figure 5) [*Boekhout et al*., 2012].

In the northwesternmost domain (between San Juan de Marcona and Atiquipa), all apatite fission-track ages overlap within uncertainty at ~60–65 Ma (Figure 5). At the NW end of the Atico-Mollendo block, older apatite fission-track ages cluster at ~90 Ma, but there is no known ~90 Ma intrusive in the area. From there, apatite fission-track ages progressively decrease along the Atico-Mollendo block toward the SE to around 60 Ma in the Mollendo area (Figure 5).

The plot of apatite fission-track ages projected along the coastline (Figure 5) shows two lateral age shifts between 60 and 90 Ma. The first is located at the vicinity of the Atiquipa fault. The second age shift, albeit less well defined than the first one, occurs NW of the Río Tambo valley and corresponds to the Río Tambo fault system (Figure 5). Both of these fault zones strike perpendicular to the trench.

Table 3. Zircon Fission-Track Analysis Results[a]

Sample	Lithology	Lat. (°S)	Long. (°W)	Elev. (m)	Central Age (Ma)	2σ Error (Ma)	*N*	Nd	ρd (10^5)	rse (ρd)	U (ppm)	$P(\chi^2)$ (%)	*D* (%)
1 M04	Proterozoic migmatite	16.87171	72.02515	1180	149	39	19	7335	1.83	1.21	78.8	93	0
1 M05	Proterozoic migmatite	16.91787	72.04906	863	194	41	20	9115	2.14	1.4	92.6	89	0
1 M06	Proterozoic migmatite	16.95583	72.05595	565	145	38	20	9115	2.15	1.38	140.9	43	17
1 M07	Proterozoic migmatite	16.98230	72.07451	280	148	40	19	7335	1.84	1.2	96.7	64	2
1 M08	Proterozoic migmatite	16.99694	72.10288	5	227	65	20	9115	2.15	1.33	78.3	31	19
1 M47	Ordovician gneiss	17.46560	71.37315	0	61	13	20	7335	1.88	1.17	289.4	12	9
1 M50	Undated granite	17.10783	71.90193	5	128	70	7	9115	2.21	1.06	199.4	0	112
1 M66	Ordovician granite	16.93880	71.59349	30	110	28	20	7335	1.92	1.19	81.1	19	22
1 M72	Ordovician granite	16.57268	72.62976	600	244	62	16	9115	2.24	1.07	100.2	66	3

[a]Age determinations were performed with $\zeta = 128 \pm 9$ for glass dosimeter CN1 according to protocol defined in text. *N*, number of grains counted; Nd, number of tracks counted to determine the reported fluence; ρd, dosimeter track density (fluence) in tracks per square centimeter; rse(ρd), relative standard error on fluence; U, uranium content (ppm); $P(\chi^2)$, probability that the single-grain ages represent one population; *D*, age dispersion.

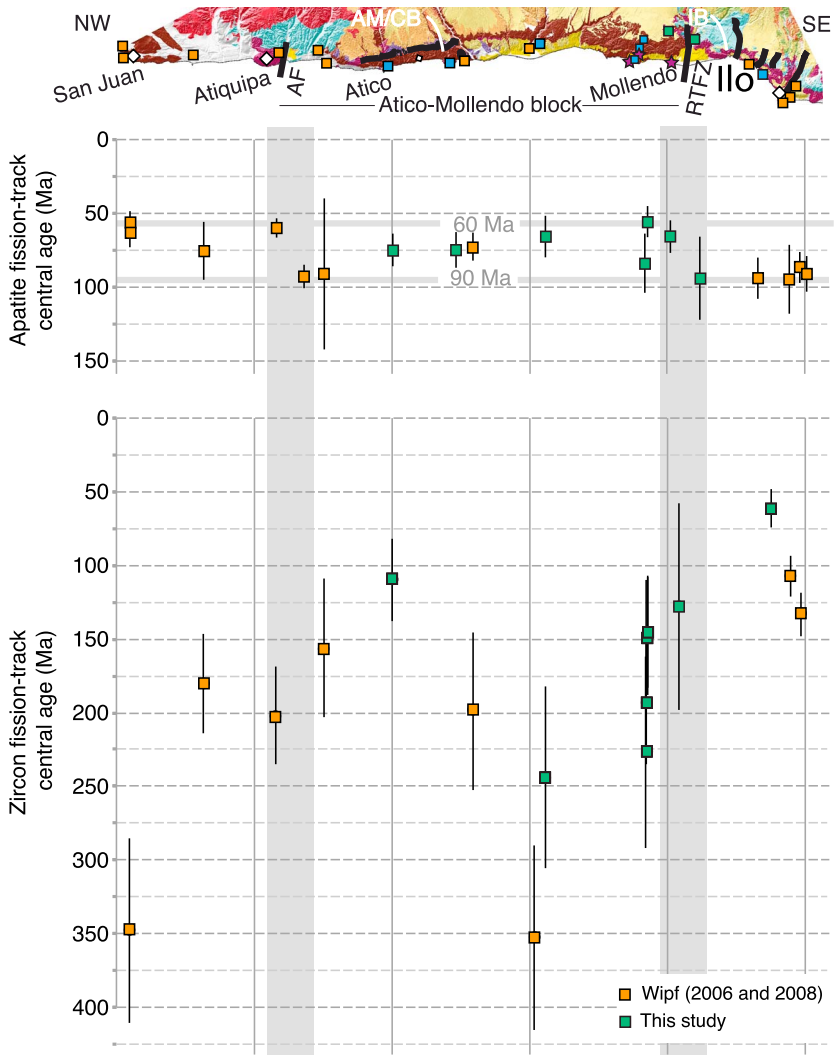

Figure 5. Synthetic figure showing the map of the coastal area of Southern Peru with our sampling sites and those by *Wipf et al.* [2008] and *Wipf* [2006, unpublished PhD] (same caption as Figure 1) together with lateral variations along the coast of (a) zircon fission-track ages and (b) apatite fission-track ages. The grey boxes indicate the position of the lateral shifts in ages that correspond to the Atiquipa Fault and the Río Tambo Fault Zone, respectively, at the NW and SE boundaries of the Atico-Mollendo block. AM, CB, and IB stand for Arequipa Massif and Coastal Belt (brown) and Ilo Batholith (purple), respectively.

Table 4. Apatite Fission-Track Analysis Results[a]

Sample	Lithology	Lat. (°S)	Long. (°W)	Elev. (m)	Central Age (Ma)	2σ Error (Ma)	*N*	Nd	ρd (10^5)	rse (ρd)	U (ppm)	*P*(χ^2) (%)	*D* (%)
1 M06	Proterozoic migmatite	16.95583	72.05595	565	55	10.5	19	8323	6.01	1.13	37.7	25	13
1 M08	Proterozoic migmatite	16.99694	72.10288	5	83	20	20	7814	5.91	1.44	8.0	29	21
1 M50	Undated granite	17.10783	71.90193	5	63	10	24	7814	6.1	1.13	13.5	37	9
1 M51	Jurassic granite	17.03928	71.69701	171	93	28	12	8965	7.1	1.07	9.0	42	5
1 M61	Jurassic granitoïd	16.89878	71.84192	1125	65	11	20	8323	6.13	1.13	13.5	32	9
1 M66	Ordovician granite	16.9388	71.59349	30	74	11	19	7814	6.16	1.15	37.5	11	12
1 M68	Undated granite	16.41116	73.23413	0	74	12	20	7814	6.19	1.18	16.8	71	1
1 M72	Ordovician granite	16.57268	72.62976	600	65	14	19	8965	6.82	1.27	12.4	29	13

[a]All fission-track age determinations were performed with $\zeta = 254 \pm 12$ for glass dosimeter IRMM540 according to protocol defined in text. *N*, number of grains counted; Nd, number of tracks counted to determine the reported fluence; ρd, dosimeter track density (fluence) in tracks per cm2; rse(ρd), relative standard error on fluence U, uranium content (ppm); *P*(χ^2), probability that the single-grain ages represent one population; *D*, age dispersion.

6. Discussion

6.1. Neoproterozoic Exhumation and Ordovician Thermal Event

Neoproterozoic biotite $^{40}Ar/^{39}Ar$ ages (Table 1) in the Ocoña canyon (Figure 1), in conjunction with the 700 Ma or older glaciogenic Chiquerio Formation that was deposited over the gneisses in San Juan (Figure 2) [*Chew et al*., 2007; *Chew and Kirkland*, 2011], demonstrate that the basement has always been at a temperature $<$350°C since the Neoproterozoic (~800 Ma).

Our $^{40}Ar/^{39}Ar$ ages decrease toward the Ocoña canyon outlet (Figure 1 and Table 1), where *Cobbing et al*. [1977] reported a 539 ± 90 Ma whole rock Rb-Sr age on a foliated granite. In the same area, a zircon from another foliated granite yielded a concordant U-Pb age of 464 ± 4 Ma [*Loewy et al*., 2004]. This age was interpreted as a crystallization age, yet the granite is foliated, and the age may alternatively reflect a metamorphic event, especially considering that the two other analyzed zircons show Pb-loss [*Loewy et al*., 2004]. Moreover, near the city of Atico, *Santos et al*. [2014] obtained Neoproterozoic and Ordovician zircon U-Pb ages on a gneiss and a granite, respectively. It should also be noted that the Chiquerio Formation experienced greenschist facies metamorphism during the Early Paleozoic [*Shackleton et al*., 1979; *Chew et al*., 2007; *Chew and Kirkland*, 2011]. The Ordovician (~470 Ma) biotite and muscovite $^{40}Ar/^{39}Ar$ ages thus reflect either the emplacement of Ordovician granitoids described and dated along the Coastal Belt, for example near Mollendo [*Loewy et al*., 2004] or north of Atico [*Santos et al*., 2014], and/or a greenschist facies metamorphism that could also be related locally to emplacement of these plutons. In any case, the thermal effect of this Ordovician event in the country rocks is spatially limited to the vicinity of plutons and did not influence the whole Proterozoic gneissic basement, which at least in part remained shallower than the 350°C isotherm since the Neoproterozoic (as indicated by the two $>$750 Ma biotite $^{40}Ar/^{39}Ar$ ages in the Ocoña canyon). This interpretation is consistent with the study of *Insel et al*. [2012], which showed that in northwestern Argentina, basement rocks from the western Puna Plateau (Sierra de Macon) resided at temperatures below 200°C since ~400 Ma and confirm that some parts of the Central Andean basement remained near surface thermal conditions for more than 400 Ma.

6.2. Jurassic Magmatic Pulse

The present-day coastal belt of southern Peru was the site of intense magmatic activity from the Middle Jurassic to the Lower Cretaceous related to the intrusion of the composite Ilo Batholith (Figure 1) in two phases, from 173 to 153 Ma and 110 to 106 Ma [*Boekhout et al*., 2012]. Only two plutonic bodies intruding the Arequipa Massif that are related to this volcanic arc are known: the 162.2 ± 1.1 Ma Atiquipa diorite and a 156.3 ± 1.3 Ma diorite located ~65 km NNW of Atico [*Santos et al*., 2014]. Different thermochronometric dating techniques including $^{40}Ar/^{39}Ar$ on biotite, K/Ar on K-feldspar [*Stewart et al*., 1974], K-Ar on whole rock [*Roperch and Carlier*, 1992], and zircon (U-Th)/He [*Schildgen et al*., 2007] applied on the Atico-Mollendo block yielded similar Jurassic ages between 177 and 157 Ma, suggesting that various plutonic bodies intruded the Neoproterozoic basement of the Arequipa Massif contemporaneously with the emplacement of the Ilo Batholith. However, more support from geochemistry and other U-Pb data are needed to establish a parallel between the Arequipa Massif intrusive units and the Ilo Batholith.

We note that in the Ilo region, northwest of the Río Tambo fault zone, the Ilo Batholith intruded the basement. In contrast, southeast of this fault zone, contemporaneous plutons intruded into Jurassic strata. Moreover, southeast of the fault, no basement rock crops out. Based on these observations and assuming that these arc-related plutons emplaced at the same structural level, we infer that the Río Tambo fault zone had already been active before or during the Jurassic, exhuming the basement of the Atico-Mollendo block. These Jurassic plutons likely affected the cooling history of the fore-arc, at least locally, which may be reflected in thermochronological data.

6.3. Cooling Pattern and Partial to Total Reset of Fission-Track Ages

Our compilation of all thermochronological data available for coastal southern Peru does not show a simple age-elevation relationship (Figure S1 in the supporting information). This result is not surprising, as the analyzed samples cover a broad, faulted region. We focused on apatite and zircon fission-track ages because the available zircon and apatite (U-Th)/He ages from the literature are too scattered and because the latter can be strongly affected by recent changes in topographic relief [e.g., *Braun*, 2002].

Our results, combined with previously published data [*Wipf*, 2006; *Wipf et al*., 2008], show that zircon fission-track ages greatly vary laterally along the coast of southern Peru. In particular, zircon fission-track ages range from Ordovician to Lower Cretaceous ages (Figure 5). Younger zircon fission-track ages (175–105 Ma) occur in two zones centered on the Ilo Batholith and Atico, respectively. This pattern suggests local partial resetting of the zircon fission-track thermochronometer either due to local burial or thermal overprinting from a close intrusion (and implies total resetting of lower temperature systems). The 175–105 Ma period corresponds to an important accumulation of volcaniclastic deposits [*Boekhout et al*., 2012; *Roperch and Carlier*, 1992] in the back-arc basin that was undergoing subsidence at a rate of 3.5 km/Myr [*Boekhout et al*., 2012]. However, such deposits should have extended over a wide area and would have reset ages over a broader area than observed.

The Middle Jurassic-Early Cretaceous period is also contemporaneous with the emplacement of the Ilo Batholith in two pulses from 173 to 153 Ma and from 110 to 106 Ma [*Boekhout et al*., 2012]. The 107 ± 15 Ma zircon fission-track age and the modeled time-temperature (*t-T*) paths reported by *Wipf* [2006] indicate that the Albian plutons likely emplaced in the upper crust, cooled rapidly, and stayed at temperatures between 60 and 80°C at least from 80 Ma to 30 Ma. We interpret the 133 ± 15 Ma zircon fission-track age reported by *Wipf* [2006] as partially annealed by a pluton emplaced during the 110–106 Ma magmatic pulse.

It is more difficult to explain the 61 ± 13 Ma zircon fission-track age obtained for a mylonitic granite, which yielded a zircon U-Pb age of 446 ± 6 Ma [*Casquet et al*., 2010] north of Ilo (sample 1 M47), but it could be related to the relatively high U concentration in the zircons of this sample, leading to lower retentivity and annealing at lower temperatures [*Garver et al*., 2005]. Furthermore, secondary magnetization of Jurassic volcanic deposits of the Chocolate Formation has been attributed to a Late Cretaceous tectono-magmatic event [*Roperch and Carlier*, 1992], which may have affected the mylonitic granite and explain the observed zircon fission-track age. However, there is no evidence of Upper Cretaceous to Paleocene intrusions in the Ilo Batholith (Figure 2) [*Boekhout et al*., 2012], and we thus regard this sample as an outlier.

In the Arequipa Massif, zircons of Neoproterozoic age likely accumulated radiation damage from at least the Ordovician to the Triassic. Such damage would imply that temperatures as low as 180–220°C were needed to partially anneal the fission tracks [*Garver et al*., 2005; *Reiners and Brandon*, 2006]. Younger zircon fission-track ages centered on Atico thus likely correspond to partial resetting in the vicinity of plutons emplaced in the Arequipa Massif during the Jurassic and Lower Cretaceous. However, the emplacement of these Jurassic plutons caused only local heating that was restricted to under 220°C; otherwise, fission tracks would have been totally annealed, and we would have obtained equivalent ages all along the coastal profile. Moreover, higher-temperature systems such as $^{40}Ar/^{39}Ar$ in biotite and muscovite with partial retention zones of about 300–350°C [*Robbins*, 1972; *Hames and Bowring*, 1994; *Reiners and Brandon*, 2006] were not affected by these localized Jurassic to Early Cretaceous thermal events, as illustrated by the Proterozoic to Ordovician biotite $^{40}Ar/^{39}Ar$ plateau ages (Figure 4).

6.4. No 90–60 Ma Thermal Reset Due to the Emplacement of the Coastal Batholith

Apatite fission-track ages range between 55 and 90 Ma in the Coastal Belt. This time range corresponds to the period of emplacement of the Coastal batholith (Figure 1) during the Upper Cretaceous-Lower Paleocene. At that time, the volcanic arc was thus located in the present-day location of the Coastal Batholith, that is to say at least ~30 km east of the coastal strip that we consider here. During this period, the geothermal gradient in the Coastal Belt was likely low (<20°C/km) because isotherms are depressed above the cold subducting oceanic slab. Present-day heat flux values measured in the fore-arc of southern Peru are ~100 mW m^{-2} at Cuajone (13 km from the arc), 65 mW m^{-2} at Toquepala (25 km from the volcanic arc), and only ~44 mW m^{-2} at Marcahui and Cerro Verde, ~30 km away from active volcanoes [*Uyeda and Watanabe*, 1982; *Henry and Pollack*, 1988]. This heat flux value is associated with a steady state geotherm of 12 to 15°C/km [*Ehlers*, 2005], which is consistent with very low geothermal gradients (~10°C/km and always <20°C/km) obtained by numerical modeling [*Dumitru*, 1991].

To better understand the effects of an intrusion on the thermal history of the area, we ran a 1-D model that predicts thermal response around an intrusion in function of its width due to heat conduction [*Ehlers*, 2005]. We ran this model with different parameters. If the intrusion is only 1 km wide, there is no sensible thermal

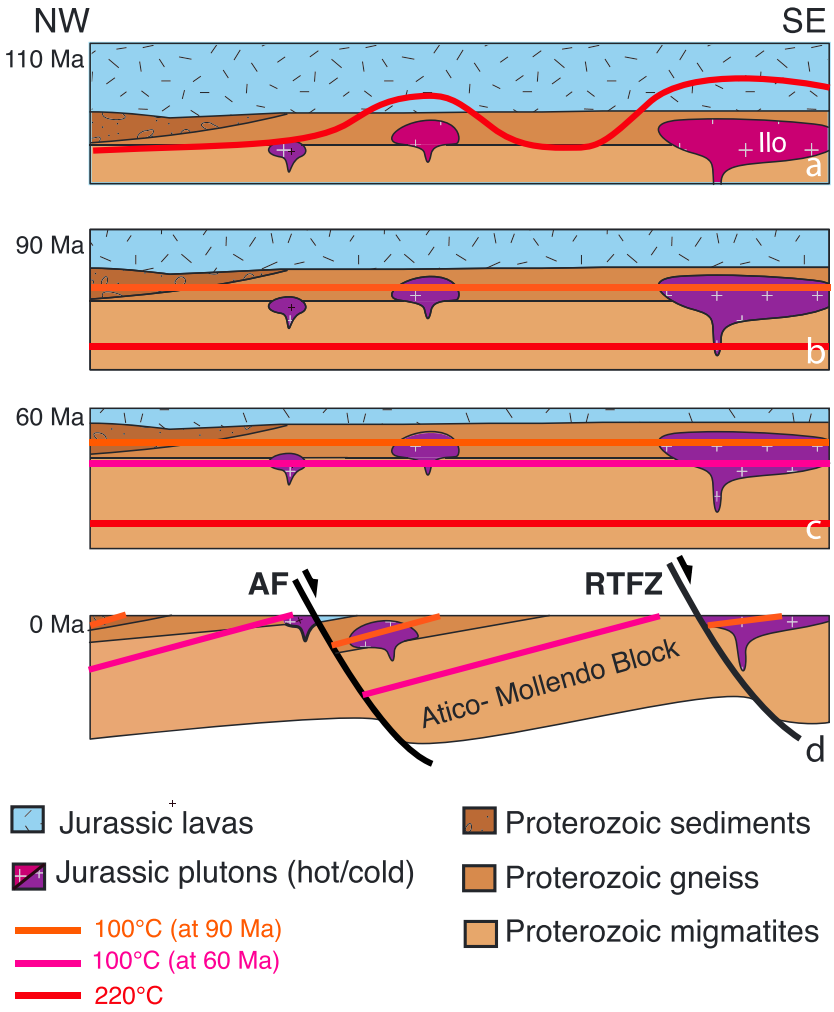

Figure 6. Evolutionary sketch showing the thermal and tectonic evolution of the Southern Peruvian fore-arc in four time steps. (a) 110 Ma: plutons intrude the Neoproterozoic basement, triggering local uplift of isotherms. (b) 90 Ma: isotherms are relaxed. (c) 60 Ma: the 90 Ma apatite fission-track central age isochrone is close to the surface and the 100°C isotherm passes through the Atiquipa diorite and the Ilo Batholith. (d) Post-35 Ma: the 90 Ma and 60 Ma apatite fission-track age isochrons are passively tilted.

effect further than 10 km. In the case of a 5 km wide intrusion, country rocks, ~30 km away from an intrusion and at an initial temperature of 100°C, are predicted to experience a maximum of 20°C heating due to the intrusion; also for this intrusion, maximum heating is attained with a delay >10 Myr and 20 Ma after the intrusion; country rocks, 30 km from the source, are still ~20°C hotter than before the intrusion. Hence, if the 90–60 Ma volcanic arc had an influence on apatite fission-track dates, it would be unlikely to observe 90 to 60 Ma apparent cooling ages. We also note that no important dykes or dyke swarms that would indicate the presence of important magmatic bodies at depth intrude the Atico-Mollendo block.

Furthermore, we find old apatite fission-track ages (e.g., ~90 Ma in Atico region; Figure 5) closest to where the magmatic arc is believed to have been located at that time, in the area that should have cooled the latest and should exhibit the youngest cooling ages if the thermochronometers were influenced by the magmatism. We are thus confident that since ~105 Ma, volcanic arc activity has not affected the apatite fission-track ages from the Coastal Belt, except in the Ilo Batholith, where apatite fission-track ages are slightly younger than crystallization ages and thus likely correspond to postemplacement cooling. The geothermal gradient in the Coastal Belt was thus probably only slightly higher than today (~15°C/km) during the Late Cretaceous-Paleocene period. Based on our previous arguments, we propose that the rocks of the Coastal Belt slowly cooled through the apatite fission-track partial annealing zone between 90 and 60 Ma.

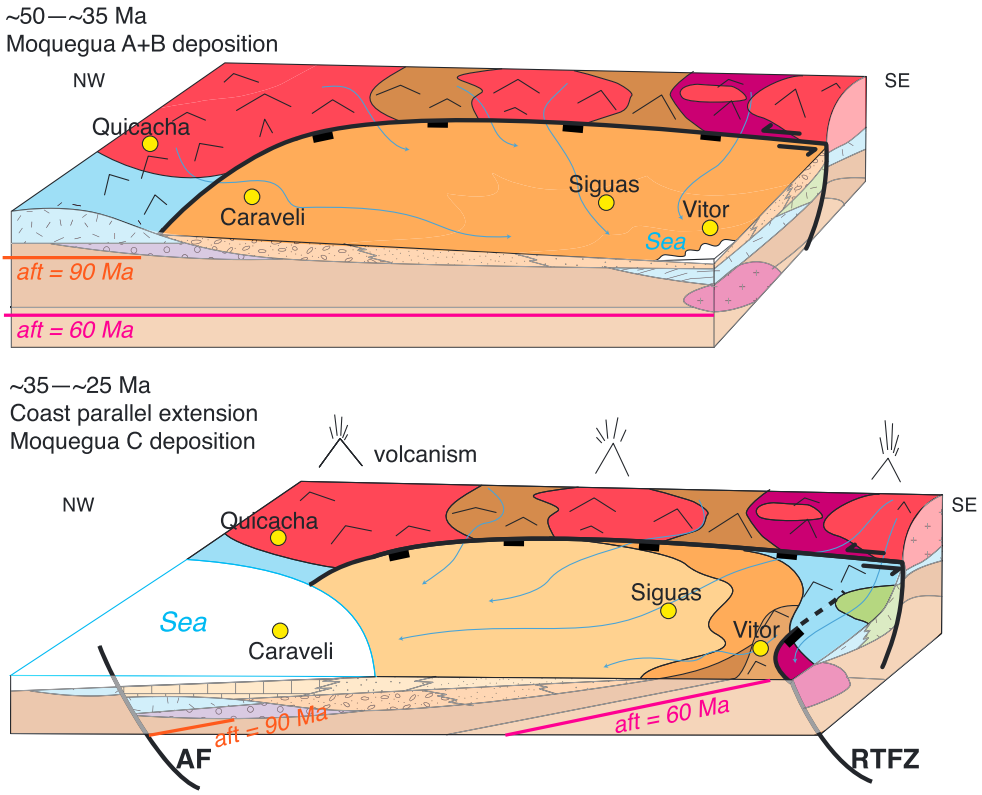

Figure 7. 3-D sketches showing the polarity of the Moquegua basin (same colors as in Figure 2). AF: Atiquipa Fault, RTFZ: Rio Tambo Fault Zone. (a) 50–35 Ma: the main faults are the Lluclla normal fault system (striking NW-SE) and Iquipi faults (SW-NE) bounding the basin onshore; sediments are prograding southeastward. At that time, the isochrons are horizontal. (b) Block tilting occurs between the AF and RTFZ. As a result, the whole Atico-Mollendo block is tilted toward the NW and the polarity of the basin switches toward the NW, as documented by the tilt of the apatite fission-track isochrons.

6.5. Postcooling Tilting of the Atico-Mollendo Block

Along the coast, apatite fission-track ages show two shifts from younger (60 Ma) to older (~90 Ma) ages that are localized across the Atiquipa and Río Tambo fault zones. Between these shifts, in the Atico-Mollendo block, the age pattern decreases toward the southeast (Figure 5). Moreover, Neoproterozoic basement evolves toward the southeast (i) from metasediments to gneisses in the hanging wall of the Atiquipa fault, (ii) from gneisses to ultrahigh-temperature (>900°C) granulites in the Atico-Mollendo block, and (iii) no Proterozoic basement crops out southeast of the Río Tambo fault zone (Figure 7). We also note that the Jurassic volcanic succession (and its underlying Pennsylvanian basin) are the thickest and best preserved in the hanging walls of the Atiquipa and Río Tambo fault zones (Figures 2 and 6).

All these observations suggest that the Atiquipa and Río Tambo fault zones divide the basement in large, crustal-scale tilted blocks (Figure 6). Moreover, because basement rocks of the Coastal Belt likely cooled slowly under 100°C between 90 and 60 Ma, we propose that the Atiquipa and Río Tambo fault zones, striking perpendicular to the coastline, were active after ~60 Ma as SW dipping normal faults that tilted the Atico-Mollendo block toward the NW (Figure 6).

The Cenozoic sedimentary archives of fore-arc deposits in the Moquegua basin provide further evidence for extension parallel to the margin (Figure 3) associated with tilting of the Atico-Mollendo block. Between 50 and ~30 Ma, the more proximal sedimentary facies of the Moquegua A/B deposits are located in the northwest portion of the Moquegua basin, whereas deposits toward the southeast are increasingly distal [*Sempere et al.*, 2004] (Figure 7a). In contrast, the Moquegua C deposits are more distal in the Caravelí region (NW portion of the basin) and more proximal toward the SE (Figure 7b). Indeed, the Caravelí limestones record a marine incursion dated at 25 Ma [*Noble et al.*, 1985], whereas Moquegua C tuffaceous volcanic strata are intercalated with fluvial conglomerates in the Siguas valley. We also note that these volcaniclastic

deposits do not appear in the Vítor valley stratigraphic succession, ~30 km SE of Siguas valley (Figure 2), suggesting that they were eroded in the southeastern area of the Moquegua basin. This architecture of the basin suggests that a paleotopographic change occurred during the early Oligocene: topographic highs sourcing the Moquegua A/B deposits that were located in the NW (Quicacha area; Figure 7) shifted to the SE (Vítor valley) during deposition of Moquegua C (Figure 7). This scenario is consistent with the sedimentological study of the fan-delta by *Alván and von Eynatten* [2014]: they proposed that these deposits (contemporaneous with the Moquegua C sediments and located ~30 km NW of the Rio Siguas outlet) record a period of coastal uplift during the Late Oligocene-Early Miocene period.

We interpret these paleotopographic changes as due to block tilting of the whole Atico-Mollendo block (Figures 6 and 7) rather than stepwise upward movement of smaller-scaled blocks separated by faults with dip and strike that would be similar to the Atiquipa and Río Tambo fault zones because of the progressive variation of apatite fission-track ages between these two fault zones. The sedimentary facies of the Eocene to early Miocene Moquegua basin permit us to infer that the tilting began before 25 Ma (based on Caravelí limestone deposits) and may have continued until at least through the early Miocene (based on coastal uplift in Camaná region [*Alván and von Eynatten*, 2014]). We also note that in the ~35 km NW of both the Atiquipa and Río Tambo fault zones (i.e., in both areas that exhumed the most), there are no preserved outcrops of Moquegua A/B and C deposits (Figure 2). This lack of preservation could be due to higher relief close to the fault zones that contributes to faster erosion compared to the rest of the tilted block.

Because all apatite fission-track ages are younger than the end of magmatism, cooling rates are equivalent to exhumation rates. For all data presented in this study, we calculated a mean cooling rate of 1.4°C/Ma, corresponding to a slow long-term exhumation rate of ~0.1 km/Myr (for a 15°C/km geothermal gradient). Assuming that this exhumation rate was constant, we thus estimate that the 30 Ma difference between the older and younger apatite fission-track ages across the Atiquipa and Río Tambo fault zones corresponds to differential exhumation of ~3 km. Moreover, considering that the distance between the two fault zones (dipping 60° toward the SE) is ~175 km, then the slip on each fault is ~1.75 km (details in Text S1 in the supporting information).

6.6. Trench-Parallel Extension and Formation of the Bolivian Orocline

Our study confirms that the Peruvian fore arc underwent trench-parallel extension from the late Eocene to the early Miocene contemporaneously to the bending of the Andean orogen. Once the orocline was formed, from Late Miocene to present, trench-perpendicular thrusts accommodating trench-parallel shortening are observed farther south (at the latitude of northern Chile). Such structures are not observed along the Peruvian fore arc and may have developed in order to accommodate strong plate coupling along the concave seaward plate boundary [*Allmendinger et al*., 2005].

Our interpretation is consistent with different paleomagnetic studies that documented clockwise and counterclockwise block rotations (around vertical axis) in northern Chile and southern Peru respectively during formation of the Bolivian Orocline [*Roperch and Carlier*, 1992; *Somoza et al*., 1999; *Roperch et al*., 2006; *Arriagada et al*., 2008; *Taylor et al*., 2005; 2007]. In particular, in their 2-D reconstruction of paleogeography, *Arriagada et al*. [2008] calculated that the oroclinal bending was accompanied by ~200 to 260 km of stretching parallel to the margin between ~10 and ~30°S during the ~45 – ~25 Ma period. The trench-perpendicular Atiquipa and Río Tambo fault zones delimiting tilted blocks that we described above thus helped accommodate coast-parallel extension in southern Peru. However, less than 5 km of extension is accommodated on these faults. The Atico-Mollendo block thus acted as a rigid block, and oroclinal bending must have been accommodated elsewhere, likely partly by the Lluclla normal fault system and in the back arc (Eastern Cordillera), as proposed by *Roperch et al*. [2006]. For example, *Eichelberger et al*. [2013] estimated that the Río Novillero Fault in Bolivia has accommodated 85 km of dextral N-S translation.

7. Conclusions

Our new geo-thermochronologic data set along the coastal southern Peru illustrates the geological evolution of the Andean fore-arc region. Together with regional geological observations, we have refined the exhumation and deformation history of the present-day fore-arc:

1. The Arequipa Massif exhumed during the Neoproterozoic, and no thermal event >350°C occurred in this area since then, except in the vicinity of plutonic intrusions during the Ordovician.
2. During the Middle Jurassic-Lower Cretaceous period, plutonic bodies intruded the Arequipa Massif contemporaneously with the emplacement of the Ilo Batholith. This lead to a moderate heating (<220°C) in restricted areas close to the plutons.
3. Since the Albian, magmatic activity has not affected cooling of rocks located in the Coastal Belt. In particular, we show that emplacement of the Coastal Batholith during the Upper Cretaceous-Paleocene period cannot be responsible for apatite fission-track ages observed in the Coastal Belt.
4. After slow cooling through the apatite fission-track partial annealing zone (100–110°C) during the Lower Cretaceous-Paleocene, the Atico-Mollendo block tilted toward the NW between two SE dipping normal faults striking perpendicular to the trench. Because paleogeographic highs sourcing the Moquegua basin sediments (located above this tilted block) migrated from the northwest during the Eocene to the southeast in the Oligocene, we propose that these normal faults accommodated the formation of the Bolivian Orocline during the Eo-Oligocene. However, the limited amount of total extension observed on these faults (<5 km) cannot account for the large amount of trench-parallel extension that is inferred from paleomagnetism studies and believed to have accommodated the oroclinal bending. Our study thus confirms that most of this extension has been accommodated somewhere besides the Peruvian fore-arc.

Acknowledgments
We thank F. Cœur and F. Sénebier for mineral separations; E. Hardwick and M. Balvay for their valuable help within the ISTerre fission-track laboratory, A. Ulianov and U. Schaltegger for their help with zircon U-Pb analysis, and M. Pringle for the help with $^{40}Ar/^{39}Ar$ analysis. This work was supported by the INSU Syster program and by the "Institut de Recherche pour le Développement" (IRD). M. Noury and M. Philippon warmly thank their research team for their financial support of publication fees. ISTerre is part of Labex OSUG@2020 (ANR10 LABX56). We thank D. Chew and an anonymous reviewer for their constructive comments and suggestions that greatly improve the manuscript. We also thank Claudio Faccenna for editorial handling of the manuscript. Supporting data are included as text, figure, and table in the supporting information file.

References

Allmendinger, R. W., G. González, J. Yu, G. Hoke, and B. Isacks (2005), Trench-parallel shortening in the Northern Chilean Forearc: Tectonic and climatic implications, *GSA Bull.*, *117*, 89–104, doi:10.1130/B25505.

Alván, A., and H. von Eynatten (2014), Sedimentary facies and stratigraphic architecture in coarse-grained deltas: Anatomy of the Cenozoic Camaná Formation, southern Peru (16°25'S to 17°15'S), *J. South Am. Earth Sci.*, *54*, 82–108, doi:10.1016/j.jsames.2014.04.008.

Armijo, R., R. Lacassin, A. Coudurier-Curveur, and D. Carrizo (2015), Coupled tectonic evolution of Andean orogeny and global climate, *Earth Sci. Rev.*, *143*, 1–35, doi:10.1016/j.earscirev.2015.01.005.

Arriagada, C., P. Roperch, C. Mpodozis, and P. R. Cobbold (2008), Paleogene building of the Bolivian Orocline: Tectonic restoration of the central Andes in 2-D map view, *Tectonics*, *27*, TC6014, doi:10.1029/2008TC002269.

Bellido, E., and C. Guevara (1963), Geología de los cuadrángulos de Punta de Bombón y Clemesí.Carta Geológica Nacional. Bol. No 5 Serie A. Ingemmet. Lima.

Boekhout, F., R. Spikings, T. Sempere, M. Chiaradia, A. Ulianov, and U. Schaltegger (2012), Mesozoic arc magmatism along the southern Peruvian margin during Gondwana breakup and dispersal, *Lithos*, *146–147*, 48–64, doi:10.1016/j.lithos.2012.04.015.

Boekhout, F., T. Sempere, R. Spikings, and U. Schaltegger (2013), Late Paleozoic to Jurassic chronostratigraphy of coastal southern Peru: Temporal evolution of sedimentation along an active margin, *J. South Am. Earth Sci.*, *47*, 179–200, doi:10.1016/j.jsames.2013.07.003.

Braun, J. (2002), Estimating exhumation rate and relief evolution by spectral analysis of age–elevation datasets, *Terra Nova*, *14*(3), 210–214.

Casquet, C., C. M. Fanning, M. d. C. Galindo Francisco, R. J. Pankhurst, C. W. Rapela, and P. Torres (2010), The Arequipa Massif of Peru: New SHRIMP and isotope constraints on a Paleoproterozoic inlier in the Grenvillian orogen, *J. South Am. Earth Sci.*, *29*, 128–142, doi:10.1016/j.jsames.2009.08.009.

Chew, D., and C. Kirkland (2011), The Chiquerío Formation, southern Peru, in *The Geological Record of Neoproterozoic Glaciations*, edited by E. Arnaud, G. P. Halverson, and G. Shields-Zhou, *Geol. Soc. London, Mem.*, 36, pp. 481–486.

Chew, D., C. Kirkland, U. Schaltegger, and R. Goodhue (2007), Neoproterozoic glaciation in the Proto-Andes: Tectonic implications and global correlation, *Geology*, *35*(12), 1095–1098, doi:10.1130/G23768A.1.

Cobbing, E. J., and W. S. Pitcher (1972), The Coastal Batholith of central Peru, *J. Geol. Soc.*, *128*(5), 421–454, doi:10.1144/gsjgs.128.5.0421.

Cobbing, E. J., J. M. Ozard, and N. J. Snelling (1977), Reconnaissance geochronology of the crystalline basement rocks of the Coastal Cordillera of southern Peru, *Geol. Soc. Am. Bull.*, *88*(2), 241–246, doi:10.1130/0016-7606(1977)88<241:RGOTCB>2.0.CO;2.

Decou, A., H. von Eynatten, M. Mamani, T. Sempere, and G. Wörner (2011), Cenozoic forearc basin sediments in Southern Peru (15–18°S): Stratigraphic and heavy mineral constraints for Eocene to Miocene evolution of the Central Andes, *Sediment. Geol.*, *237*(1), 55–72, doi:10.1016/j.sedgeo.2011.02.004.

Decou, A., H. von Eynatten, I. Dunkl, D. Frei, and G. Wörner (2013), Late Eocene to Early Miocene Andean uplift inferred from detrital zircon fission track and U-Pb dating of Cenozoic forearc sediments (15–18°S), *J. South Am. Earth Sci.*, *45*, 6–23, doi:10.1016/j.jsames.2013.02.003.

Demouy, S., J.-L. Paquette, M. de Saint Blanquat, M. Benoit, E. A. Belousova, S. Y. O'Reilly, F. García, L. C. Tejada, R. Gallegos, and T. Sempere (2012), Spatial and temporal evolution of Liassic to Paleocene arc activity in southern Peru unraveled by zircon U-Pb and Hf in-situ data on plutonic rocks, *Lithos*, *155*, 183–200, doi:10.1016/j.lithos.2012.09.001.

Dumitru, T. A. (1991), Effects of subduction parameters on geothermal gradients in forearcs, with an application to Franciscan Subduction in California, *J. Geophys. Res.*, *96*(B1), 621–641, doi:10.1029/90JB01913.

Dumitru, T. A. (1993), A new computer-automated microscope stage system for fission-track analysis, *Nucl. Tracks Radiat. Meas.*, *21*(4), 575–580, doi:10.1016/1359-0189(93)90198-I.

Ehlers, T. A. (2005), Crustal thermal processes and the interpretation of thermochronometer data, *Rev. Mineral. Geochem.*, *58*(1), 315–350, doi:10.2138/rmg.2005.58.12.

Eichelberger, N., N. McQuarrie, T. A. Ehlers, E. Enkelmann, J. B. Barnes, and R. O. Lease (2013), New constraints on the chronology, magnitude, and distribution of deformation within the central Andean orocline, *Tectonics*, *32*, 1432–1453, doi:10.1002/tect.20073.

Flores, A., J. Acosta, C. Bedoya, and T. Sempere (2005), Oligocene-Neogene tectonics and sedimentation in the forearc of southern Peru, Tacna area (17.5°–18. 5°S) 6th International Symposium on Andean Geodynamics 12-14 Septembre 2005, IRD Edts., Paris.

Galbraith, R. F. (2005), *Statistics for Fission Track Analysis*, pp. 224, Chapman and Hall/CRC Press, London ISBN 9781584885337.

Garver, J. I., P. W. Reiners, L. J. Walker, J. M. Ramage, and S. E. Perry (2005), Implications for timing of Andean uplift from thermal resetting of radiation damaged zircon in the Cordillera Huayhuash, Northern Peru, *J. Geol.*, *113*(2), 117–138, doi:10.1086/427664.

Google Earth (2014), Northwestern corner: 75°W;15°S; southeaster corner: 71°W,18°S NW SE images dated from April 2013, last consulted August 28th 2014.
Green, D. H. (1981), Petrogenesis of Archaean ultramafic magmas and implications for Archaean tectonics, *Dev. Precambrian Geol.*, *4*, 469–489, doi:10.1016/S0166-2635(08)70024-0.
Gunnell, Y., J.-C. Thouret, S. Brichaud, A. Carter, and K. Gallagher (2010), Low-temperature thermochronology in the Peruvian Central Andes: Implications for long-term continental denudation, timing of plateau uplift, canyon incision and lithosphere dynamics, *J. Geol. Soc.*, *167*, 803–815, doi:10.1144/0016-76492009-166A.
Hall, S. R., D. L. Farber, L. Audin, and R. C. Finkel (2012), Recently active contractile deformation in the forearc of southern Peru, *Earth Planet. Sci. Lett.*, *337*, 85–92, doi:10.1016/j.epsl.2012.04.007.
Hames, W. E., and S. A. Bowring (1994), An empirical evaluation of the argon diffusion geometry in muscovite, *Earth Planet. Sci. Lett.*, *124*(1–4), 161–169, doi:10.1016/0012-821X(94)00079-4.
Henry, S. G., and N. H. Pollack (1988), Terrestrial heat flow above the Andean subduction zone in Boliviaand Peru, *J. Geophys. Res.*, *93*(B12), 15,153–15,162, doi:10.1029/JB093iB12p15153.
Insel, N., C. J. Poulsen, T. A. Ehlers, and C. Sturm (2012), Response of meteoric δ 18 O to surface uplift—Implications for Cenozoic Andean Plateau growth, *Earth Planet. Sci. Lett.*, *317*, 262–272, doi:10.1016/j.epsl.2011.11.039.
Isacks, B. L. (1988), Uplift of the Central Andean plateau and Bending of the Bolivian Orocline, *J. Geophys. Res.*, *93*(B4), 3211–3231, doi:10.1029/JB093iB04p03211.
Jacay, J., T. Sempere, L. Husson, and A. Pino (2002), Structural characteristics of the Incapuquio fault system, southern Peru in *Andean Geodynamics : Extended Abstracts*, 5th International Symposium on Andean Geodynamics, IRD edts., Toulouse, pp. 319–321.
James, D. E. (1971), Plate tectonic model for the evolution of the Central Andes, *Geol. Soc. Am. Bull.*, *82*(12), 3325–3346, doi:10.1130/0016-7606(1971)82[3325:PTMFTE]2.0.CO;2.
James, D. E., and I. S. Sacks (1999), Cenozoic formation of the Central Andes: A geophysical perspective, *Geol. Ore Deposits Cent. Andes*, *7*, 1–25.
Jenks, W. (1948), Geología de la Hoja de Arequipa al 200,000, *Instituto geológico del Perú Boletín*, *9*, 1–104.
Kono, M., Y. Fukao, and A. Yamamoto (1989), Mountain building in the Central Andes, *J. Geophys. Res.*, *94*(B4), 3891–3905, doi:10.1029/JB094iB04p03891.
Koppers, A. A. P. (2002), ArArCALC: Software for 40Ar/39Ar age calculations, *Comput. Geosci.*, *28*, 605–619, doi:10.1016/S0098-3004(01)00095-4.
Loewy, S. L., J. N. Connelly, and I. W. D. Dalziel (2004), An orphaned basement block: The Arequipa-Antofalla Basement of the central Andean margin of South America, *Geol. Soc. Am. Bull.*, *116*(1-2), 171–187, doi:10.1130/B25226.1.
Mamani, M., G. Wörner, and T. Sempere (2010), Geochemical variations in igneous rocks of the Central Andean orocline (13°S to 18°S): Tracing crustal thickening and magma generation through time and space, *Geol. Soc. Am. Bull.*, *122*(1–2), 162–182, doi:10.1130/B26538.1.
Marocco, R. (1984), Dynamique du remplissage d'un bassin intramontagneux cénozoïque andin: Le bassin Moquegua (Sud du Pérou), *Cahiers ORSTOM. Série Géologie*, *14*(2), 117–140 ISSN 0029-7232.
Martignole, J., and J.-E. Martelat (2003), Regional-scale Grenvillian-age UHT metamorphism in the Mollendo-Camana block (basement of the Peruvian Andes), *J. Metamorph. Geol.*, *21*(1), 99–120, doi:10.1046/j.1525-1314.2003.00417.x.
Mégard, F. (1978), Etude géologique des Andes du Pérou central: Memoire ORSTROM no. 86.
Moores E., and R. J., Twiss (1995), *Tectonics*, W. H. Freeman, ISBN 0-7167-2437-5.
Myers, J. S. (1975), Vertical crustal movements of the Andes in Peru, *Nature*, *254*, 672–674.
Narvaez, S. (1964), *Geología de los cuadrángulos de Ilo y Locumba (Hojas 36-t y 36-u)*. INGEMMET, Boletín. Serie A: Carta Geológica Nacional, 7, 75 p., 2 mapas.
Noble, D. C., M. Sébrier, F. Megard, and E. H. McKee (1985), Demonstration of two pulses of Paleogene deformation in the Andes of Peru, *Earth Planet. Sci. Lett.*, *73*(2–4), 345–349, doi:10.1016/0012-821X(85)90082-2.
Ramos, V. A., and A. Aleman (2000), Tectonic evolution of the Andes, in *Tectonic Evolution of South America*, edited by Cordani et al., pp. 453–480, 31st Int. Geol. Congress, Río de Janeiro, Brazil.
Reiners, P. W. (2005), Zircon (U-Th)/He thermochronometry, *Rev. Mineral. Geochem.*, *58*(1), 151–179.
Reiners, P. W., and M. T. Brandon (2006), Using thermochronology to understand orogenic erosion, *Annu. Rev. Earth Planet. Sci.*, *34*, 419–466, doi:10.1146/annurev.earth.34.031405.125202.
Reiners, P. W., T. L. Spell, S. Nicolescu, and K. A. Zanetti (2004), Zircon (U-Th)/He thermochronometry: He diffusion and comparisons with 40 Ar/39 Ar dating, *Geochim. Cosmochim. Acta*, *68*(8), 1857–1887, doi:10.1016/j.gca.2003.10.021.
Renne, P. R., C. C. Swisher, A. L. Deino, D. B. Karner, T. L. Owens, and D. J. DePaolo (1998), Intercalibration of standards, absolute ages and uncertainties in 40Ar/39Ar dating, *Chem. Geol.*, *145*, 117–152, doi:10.1016/S0009-2541(97)00159-9.
Robbins, G. A. (1972), Radiogenic argon diffusion in muscovite under hydrothermal conditions MS thesis, Brown Univ., Providence, R. I.
Rochat, P., G. Hérail, P. Baby, and G. Mascle (1999), Bilan crustal et contrôle de la dynamique érosive et sédimentaire sur les mécanismes de formation de l'Altiplano, *C. R. Acad. Sci.*, *328*(3), 189–195, doi:10.1016/S1251-8050(99)80095-0.
Roperch, P., and G. Carlier (1992), Paleomagnetism of Mesozoic rocks from the central Andes of southern Peru: Importance of rotations in the development of the Bolivian Orocline, *J. Geophys. Res.*, *97*(B12), 17,233–17,249, doi:10.1029/92JB01291.
Roperch, P., T. Sempere, O. Macedo, C. Arriagada, M. Fornari, C. Tapia, and C. Laj (2006), Counterclockwise rotation of late Eocene-Oligocene fore-arc deposits in southern Peru and its significance for oroclinal bending in the central Andes, *Tectonics*, *25*, TC3010, doi:10.1029/2005TC001882.
Santos, A., G. Weimin, D. Soberon, D. Torres, and W. Ccallo (2014), Magmatismo y litogeoquimica de los granitoides des jurasico y cretacico entre Chala y Atico XVII Congresso Peruano de Geologia : Resúmenes extendidos, Sociedad geológica del Perú, Lima, 4 p.
Schildgen, T. F., K. V. Hodges, K. X. Whipple, P. W. Reiners, and M. S. Pringle (2007), Uplift of the western margin of the Andean plateau revealed from canyon incision history, southern Peru, *Geology*, *35*(6), 523–526, doi:10.1130/G23532A.1.
Schildgen, T. F., K. V. Hodges, K. X. Whipple, M. S. Pringle, M. van Soest, and K. Cornell (2009), Late Cenozoic structural and tectonic development of the western margin of the central Andean Plateau in southwest Peru, *Tectonics*, *28*, TC4007, doi:10.1029/2008TC002403.
Sébrier, M., J. L. Mercier, F. Mégard, G. Laubacher, and E. Carey-Gailhardis (1985), Quaternary normal and reverse faulting and the state of stress in the central Andes of south Peru, *Tectonics*, *4*(7), 739–780, doi:10.1029/TC004i007p00739.
Sempere, T. (2000), Discussion: Sediment accumulation on top of the Andean orogenic wedge: Oligocene to late Miocene basins of the Eastern Cordillera, southern Bolivia, *Geol. Soc. Am. Bull.*, *112*, 1752–1755, doi:10.1130/0016-7606(2000)112<1752:DSAOTO>2.0.CO;2.
Sempere, T., and J. Jacay (2006), Estructura tectónica del sur del Perú (antearco, arco, y Altiplano suroccidental), in *XIII Congresso Peruano de Geologia : Resúmenes extendidos* Sociedad geológica del Perú, Lima, pp. 324–327.
Sempere, T., and J. Jacay (2007), *Synorogenic extensional tectonics in the forearc, arc and southwest Altiplano of southern Peru*, *Eos Trans. AGU*, 88(23), Joint Assembly Supplement, Abstract U51B-04.

Sempere, T., and J. Jacay (2008), Anatomy of the Central Andes: Distinguishing between western, magmatic Andes and eastern, tectonic Andes, in *7th International Symposium on Andean Geodynamics* Extended abstracts, pp. 504–507, IRD edts, Nice.

Sempere, T., F. Boekhout, M. Noury, E. Taipe, F. García, J. Jacay, R. A. Spikings, and U. Schaltegger (2012), Reinstauración del Grupo Yamayo (Bellido y Guevara, 1963), y su significado en la evolución de la margen peruana del Carbonífero al Triásico, in *Resúmenes extendidos del XVI Congresso Peruano de Geologia, Boletín 108-44*, Sociedad geológica del Perú, Lima, 5 p.

Sempere, T., et al. (2002), Late Permian-Middle Jurassic lithospheric thinning in Peru and Bolivia, and its bearing on Andean-age tectonics, *Tectonophysics*, *345*(1), 153–181, doi:10.1016/S0040-1951(01)00211-6.

Sempere, T., M. Fornari, J. Acosta, A. Flores, J. Jacay, D. Peña, P. Roperch, and E. Taipe (2004), Estratigrafía, geocronología, paleogeografía y paleotectónica de los depósitos de antearco del sur del Perú, in *Resúmenes Extendidos del XII Congreso Peruano de Geología*, pp. 533–536, Sociedad Geológica del Perú, Lima.

Shackleton, R. M., A. C. Ries, M. P. Coward, and P. R. Cobbold (1979), Structure, metamorphism an geochronology of the Arequipa Massif of coastal Peru, *J. Geol. Soc.*, *136*(2), 195–214, doi:10.1144/gsjgs.136.2.0195.

Somoza, R., S. Singer, and A. Tomlinson (1999), Paleomagnetic study of upper Miocene rocks from northern Chile: Implications for the origin of Late Miocene-Recent tectonic rotations in the southern Central Andes, *J. Geophys. Res.*, *104*, 22,923–22,936, doi:10.1029/1999JB900215.

Steiger, R., and E. Jäger (1977), Subcommission on geochronology: Convention on the use of decay constants in geo-and cosmochronology, *Earth Planet. Sci. Lett.*, *36*(3), 359–362, doi:10.1016/0012-821X(77)90060-7.

Stewart, J. W., J. F. Evernden, and N. J. Snelling (1974), Age determinations from Andean Peru: A reconnaissance survey, *Geol. Soc. Am. Bull.*, *85*(7), 1107–1116, doi:10.1130/0016-7606(1974)85<1107:ADFAPA>2.0.CO;2.

Suárez, G., P. Molnar, and B. C. Burchfield (1983), Seismicity, fault plane solutions, depth of faulting, and active tectonics of the Andes of Peru, Ecuador, and southern Colombia, *J. Geophys. Res.*, *88*(B12), 10,403–10,428, doi:10.1029/JB088iB12p10403.

Taylor, G. K., B. Dashwood, and J. Grocott (2005), Central Andean rotation pattern: Evidence from paleomagnetic rotations of an anomalous domain in the forearc of northern Chile, *Geology*, *33*(10), 777–780, doi:10.1130/G21876.1.

Taylor, G. K., J. Grocott, B. Dashwood, M. Gipson, and C. Arévalo (2007), Implications for crustal rotation and tectonic evolution in the central Andes fore arc: New paleomagnetic results from the Copiapó region of northern Chile, 26°–28°S, *Tectonics*, *112*, B01102, doi:10.1029/2005JB003950.

Tosdal, R. M., A. H. Clark, and E. Farrar (1984), Cenozoic polyphase landscape and tectonic evolution of the Cordillera Occidental, southernmost Peru, *Geol. Soc. Am. Bull.*, *95*(11), 1318–1332, doi:10.1130/0016-7606(1984)95<1318:CPLATE>2.0.CO;2.

Ulianov, A., O. Müntener, U. Schaltegger, and F. Bussy (2012), The data treatment dependent variability of U-Pb zircon ages obtained using mono-collector, sector field, laser ablation ICPMS, *J. Anal. At. Spectrom.*, *27*(4), 663–676, doi:10.1039/C2JA10358C.

Uyeda, S., and T. Watanabe (1982), Terrestrial heat flow in western South America, *Tectonophysics*, *83*(1–2), 63–70, doi:10.1016/0040-1951(82)90007-5.

Vermeesch, P. (2009), Radialplotter: A java application for fission track, luminescence and other radial plots, *Radiat. Meas.*, *44*(4), 409–410, doi:10.1016/j.radmeas.2009.05.003.

Vermeesch, P. (2012), On the visualisation of detrital age distributions, *Chem. Geol.*, *312–313*, 190–194, doi:10.1016/j.chemgeo.2012.04.021.

Wipf, M. A. (2006), Evolution of the Western Cordillera and Coastal Margin of Peru: Evidence from low-temperature thermochronology and geomorphology PhD thesis, Swiss Federal Institute of Technology.

Wipf, M. A., G. Zeilinger, D. Seward, and F. Schlunegger (2008), Focused subaerial erosion during ridge subduction: Impact on the geomorphology in south-central Peru, *Terra Nova*, *20*(1), 1–10, doi:10.1029/1999JB900215.

York, D. (1969), Least squares fitting of a straight line with correlated errors, *Earth Planet. Sci. Lett.*, *5*, 320–324, doi:10.1016/S0012-821X(68)80059-7.